Electronic Supplementary Information (ESI)

Ultralong life and high capacity magnesium/sodium hybrid-ion battery using ternary $CoSe/NiSe_2/CuSe_2$ cathode and dual-ion electrolyte

Ting Zhou[a], Yajun Zhu[a], Yun Shen[b], Hui Qiu[b], Tianli Han[a], Jinjin Li[*,c], Jinyun Liu[*,a]

Experimental

Preparation of CoNiCu-precursor. All chemical drugs are analyzed for purity and can be used directly without purification. The precursor was synthesized by one step hydrothermal method. 0.267 mmol $Ni(NO_3)_2•6H_2O$ (99%, Aladdin), 0.533 mmol $Co(NO_3)_2•6H_2O$ (99%, Aladdin), 0.2 mmol $Cu(NO_3)_2•3H_2O$ (99%, Aladdin), and 0.3 mmol urea (98%, Aladdin) were put into 40 mL deionized water and stirred to dissolve for 30 min. The transparent solution was transferred to a 50 mL Teflon lined stainless steel autoclave and kept at 120 °C for 10 h, and then cooling and washing before use.

Preparation of $CoSe/NiSe_2/CuSe_2$ (CNCS). The 0.1 g CoNiCu-precursor was ultrasonically dispersed in a mixed solution of 20 mL H_2O and 20 mL ethanol. At the same time, sufficient amount of selenium powder (Se, 99%, Aladdin) was stirred and dissolved in 5 mL hydrazine hydrate solution in a water bath at 80 °C, and then the selenium solution was added drop by drop to the above solution. After 10 min of ultrasound, the solution was kept in the oven at 180 °C for 12 h, and finally the $CoSe/NiSe_2/CuSe_2$ sample was obtained.

Preparation the dual-ion electrolyte. 0.152 g of anhydrous magnesium chloride

($MgCl_2$, 98%, Aladdin) and 0.215 g of aluminum chloride ($AlCl_3$, 98%, Aladdin) were dissolved and stirred in 4 mL of triethylene glycol dimethyl ether (TGM) overnight to obtain 0.2 M $[Mg_2Cl_2][AlCl_4]_2$ solution. Then 0.4 M NaTFSI additive was added to the above solution and stirred for 12 h to prepare magnesium/sodium hybrid ion electrolyte. In order to compare other ether reagents, ethylene glycol dimethyl ether (DME) and diethylene glycol dimethyl ether (DGM) were replaced by TGM.

Characterizations. The morphology, size and micro-structure of the samples were analyzed by a field emission scanning electron microscopy (FESEM, Hitachi Regulus S-8100) and a transmission electron microscopy (TEM, HT-7700, 120 kV). Energy dispersive X-ray spectroscopy (EDS) was used to characterize the composition of elements on the surface of the sample and observe the distribution of elements on the surface of the sample. The crystallinity of the sample was observed under high-resolution TEM (HTEM) at acceleration voltage of 200 kV. The phase and valence state of the samples were identified by X-ray diffraction (XRD, Rigaku SmartLab, 1.54060Å) and X-ray photoelectron spectroscopy (XPS, Thermo Field, Thermo Scientific K-Alpha). Brunauer-Emmett-Teller (BET, N_2) specific surface area and pore size distribution were measured and collected on ASAP 2460 analyzer.

Preparation of electrodes. The CNCS active material, conductive carbon black (AR, 99%) and polyvinyl fluoride (PVDF, AR, 99%) binder were evenly ground and mixed in N-methyl-2-pyrrolidone (NMP, AR, 99%) with the mass ratio of 8:1:1. The obtained slurry was coated on the copper (Cu, 5 μm) foil and dried overnight in the oven at 80 °C to make the cathode. The electrode was cut into a disc with a diameter of 12 mm and the loading mass of the active material was 1.2 mg cm^{-2}. All CR2023-type coin batteries are assembled in a glovebox filled with Ar gas (Super 1220/750/900, $H_2O/O_2 < 0.01$ ppm). A polished Mg flake with a thickness of 60 um and an area of 2.0 cm^2 was used as the counter electrode, a glass fiber film (GF/F) as the diaphragm, and MACC/TGM-NaTFSI solution was used as the magnesium/sodium dual-ion electrolyte. The magnesium-based electrolyte content of each coin cell is about 100 μL.

Electrochemical measurements. A Mg|Mg symmetrical battery was assembled with Mg foil of the same area. A Mg|Cu asymmetric battery was prepared with a Cu foil as substrate of Mg plating/stripping and Mg foil as counter electrode. The cyclic voltammetry (CV) curves and electrochemical impedance spectroscopy (EIS) were collected at an electrochemical workstation (CHI660E). The galvanostatic charge-discharge profiles, rate performance and cycle property were measured on a Neware (CT-4008) tester. Using the galvanostatic interval titration technique (GITT) collected the potential response in different electrolytes at a current density of 0.2 A g^{-1} for 10 min of charging/charging, where the interval was 2 h. In the single pouch-cell, the electrolyte content was maintained at 100 μL mg^{-1}.

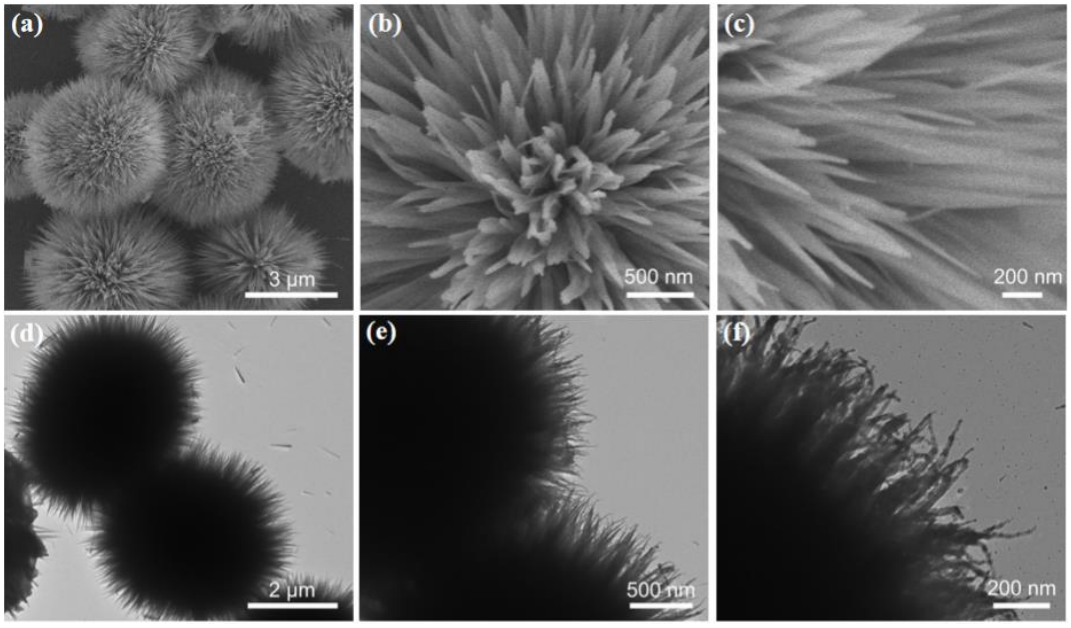

Fig. S1 (a-c) SEM and (d-f) TEM images of CoNiCu precursor.

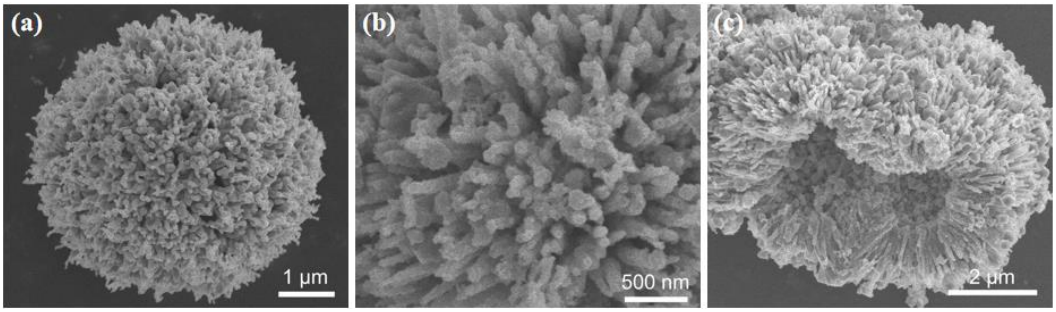

Fig. S2 (a) Low- and (b) high-magnifications SEM images of CNCS. (c) SEM image of broken sample after grinding.

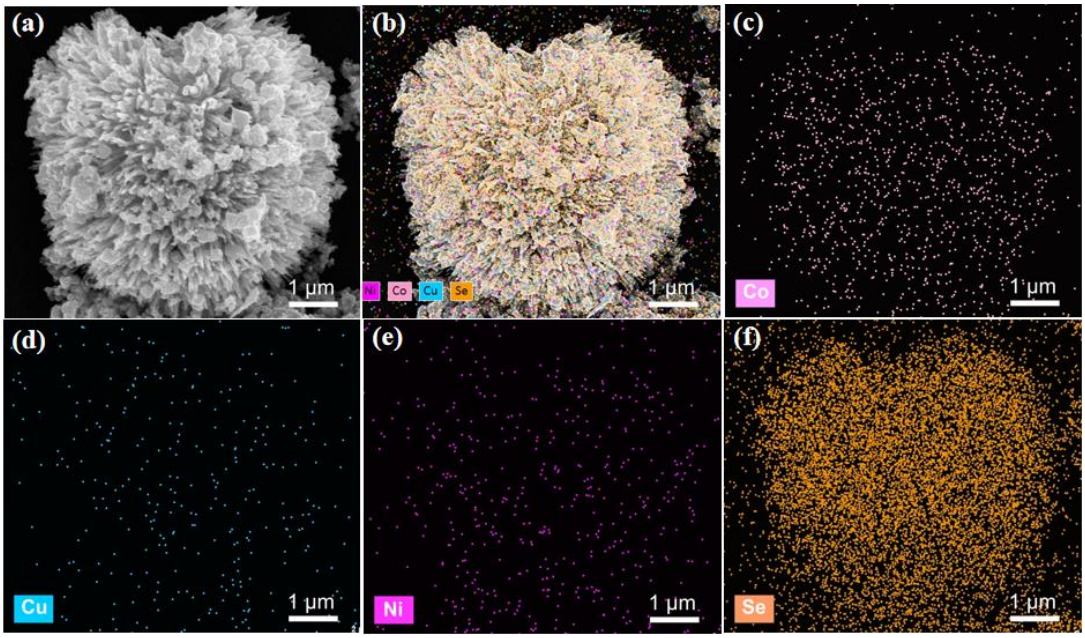

Fig. S3 (a) SEM and (b-f) elemental mapping images of the CNCS.

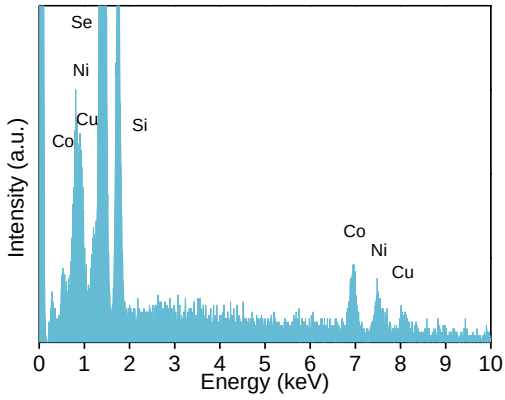

Fig. S4 EDS spectrum of the CNCS.

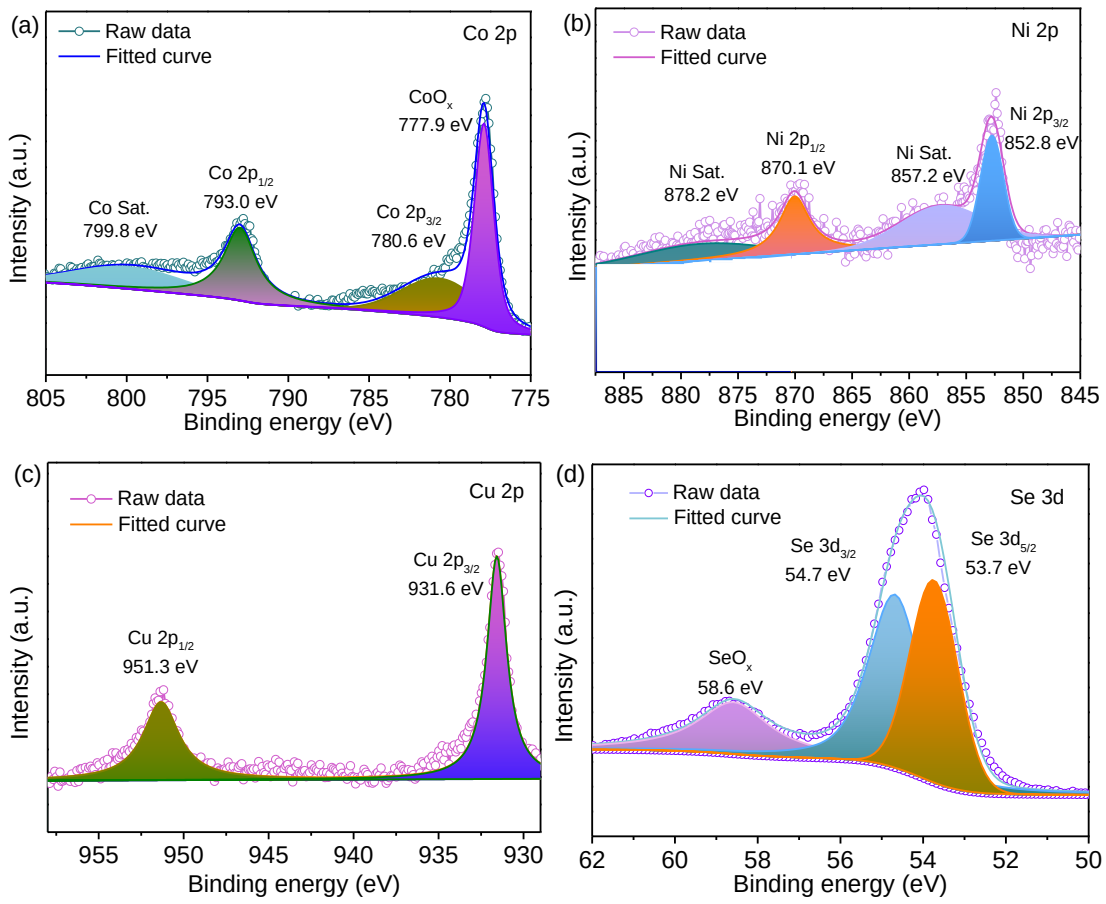

Fig. S5 XPS spectra of (a) Co 2p, (b) Ni 2p, (c) Cu 2p, and (d) Se 3d.

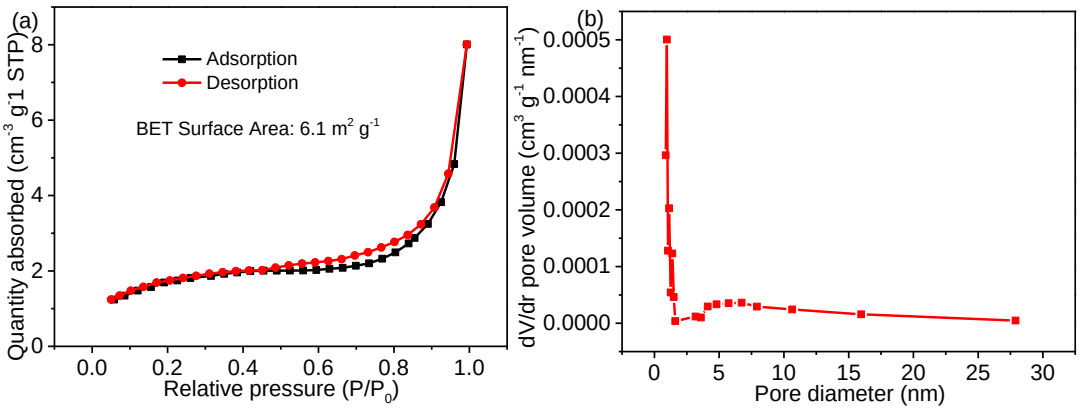

Fig. S6 (a) N_2 adsorption-desorption isotherm and (b) the corresponding pore-size distribution of the CNCS.

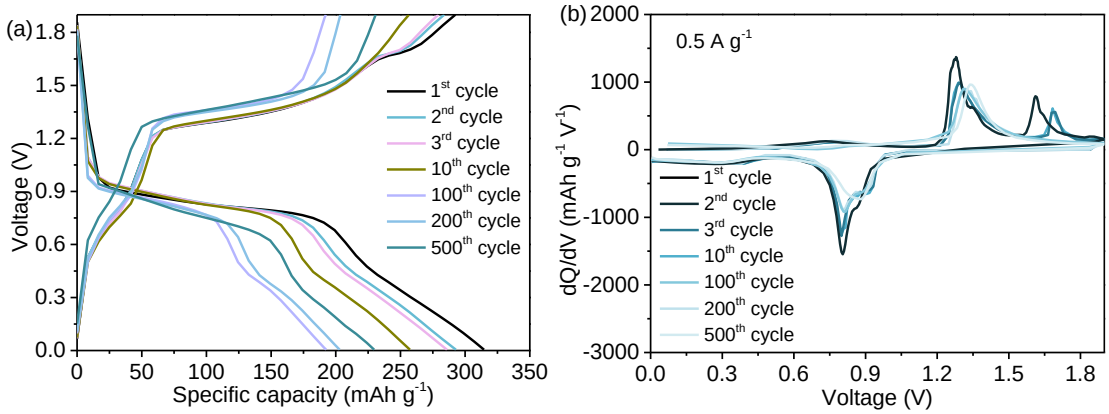

Fig. S7 (a) Galvanostatic charge/discharge profiles and (b) dQ/dV plots of MNHB at 0.5 A g^{-1}.

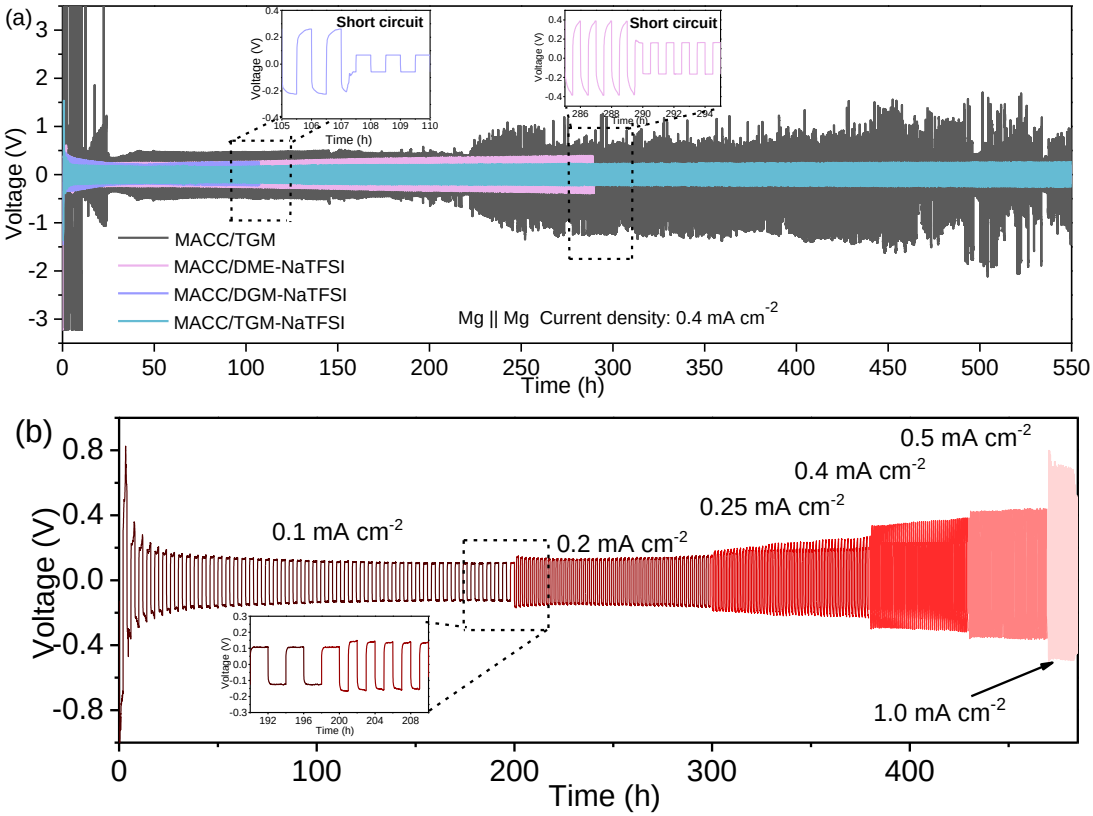

Fig. S8 The mechanism study of the MACC/TGM-NaTFSI electrolyte. (a) The symmetry Mg|Mg battery with different electrolytes at 0.4 mA cm^{-2}. (b) The symmetrical Mg|Mg battery using 0.2 M MACC/TGM-0.4 M NaTFSI electrolyte at current densities of 0.1~1.0 mA cm^{-2}.

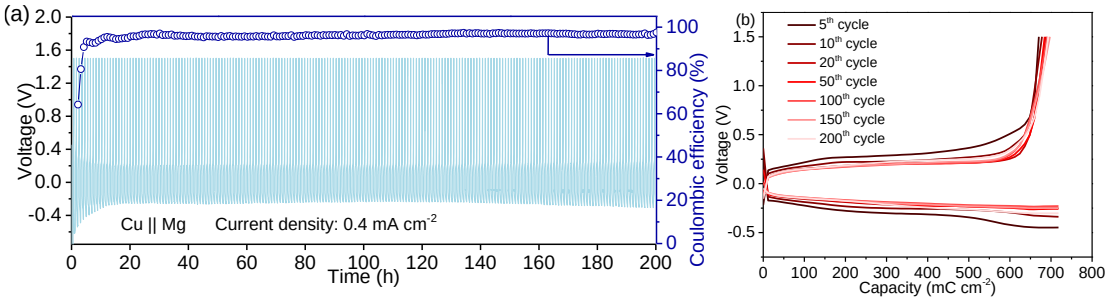

Fig. S9 (a) The time-voltage distribution curves and Coulombic efficiency of a Mg|Cu asymmetric battery in 0.2 M MACC/TGM-0.4 M NaTFSI electrolyte at 0.4 mA cm^{-2}. (b) The charge/discharge curves of the Mg|Cu asymmetric battery at 0.4 mA cm^{-2}.

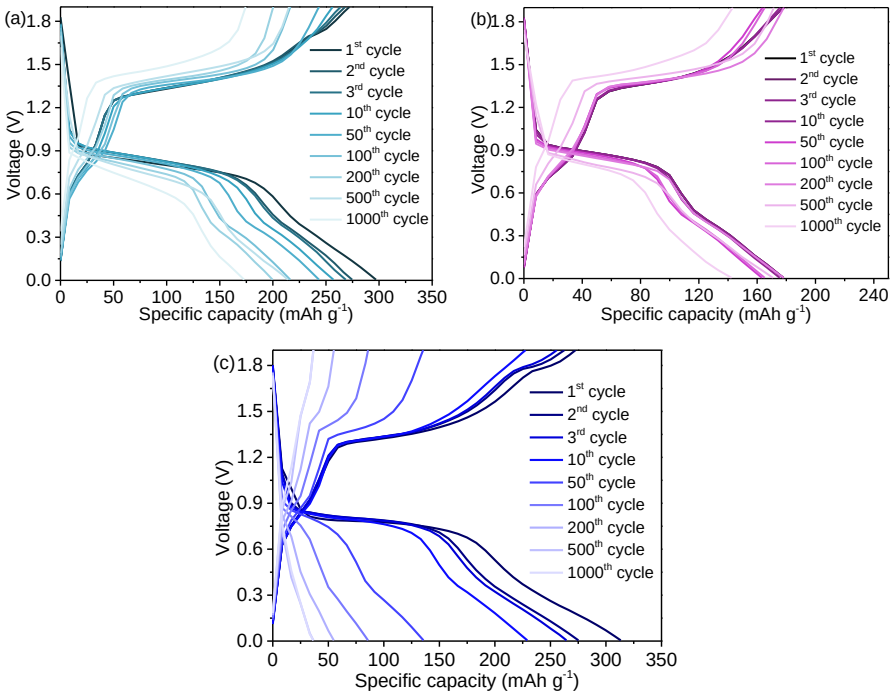

Fig. S10 Charging/discharging profiles of the MNHBs at 1.0 A g^{-1} with (a) MACC/TGM-NaTFSI, (b) MACC/DME-NaTFSI, and (c) MACC/DGM-NaTFSI electrolytes.

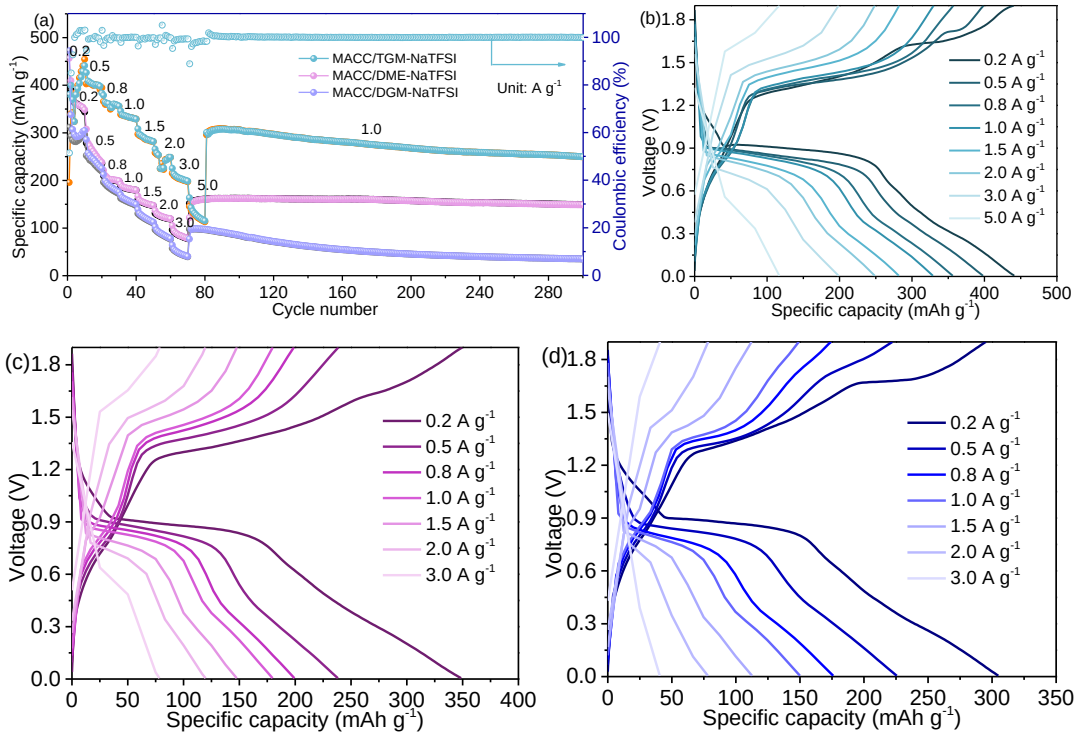

Fig. S11 (a) Comparison of rate performances using different electrolytes. (b-d) Corresponding charging/discharging curves.

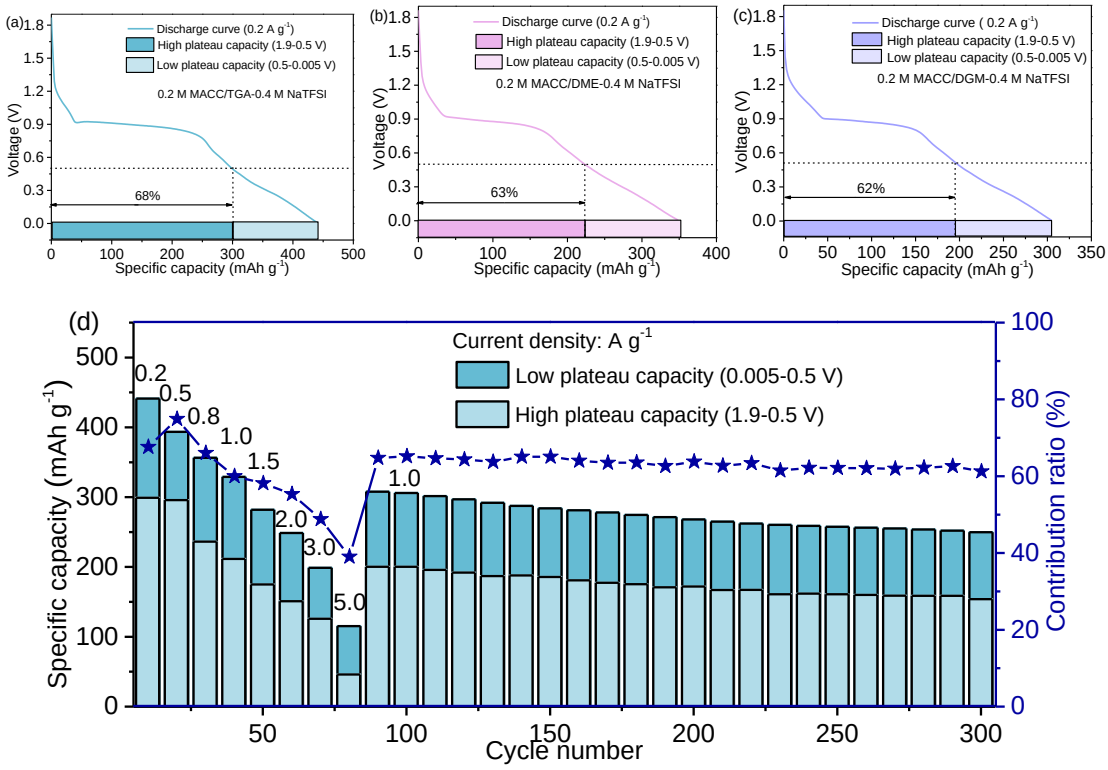

Fig. S12 Low- and high-plateau capacities of the CNCS cathodes with (a) MACC/TGM-NaTFSI, (b) MACC/DME-NaTFSI, and (c) MACC/DGM-NaTFSI

electrolytes at 0.2 A g^{-1}. The discharge curves were collected in the 10th cycles in **Fig. S11a**. (d) Contribution ratio of the high voltage plateau capacity using MACC/TGM-NaTFSI electrolyte.

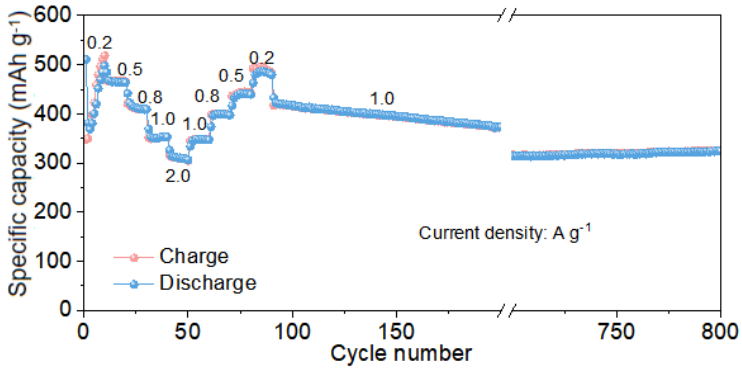

Fig. S13 The rate-performance of the MNHB.

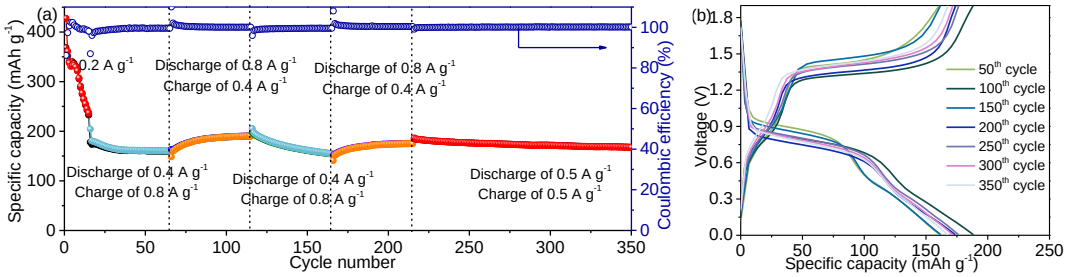

Fig. S14 (a) Cycling performance at different charging/discharging rates and (b) corresponding charge/discharge curves.

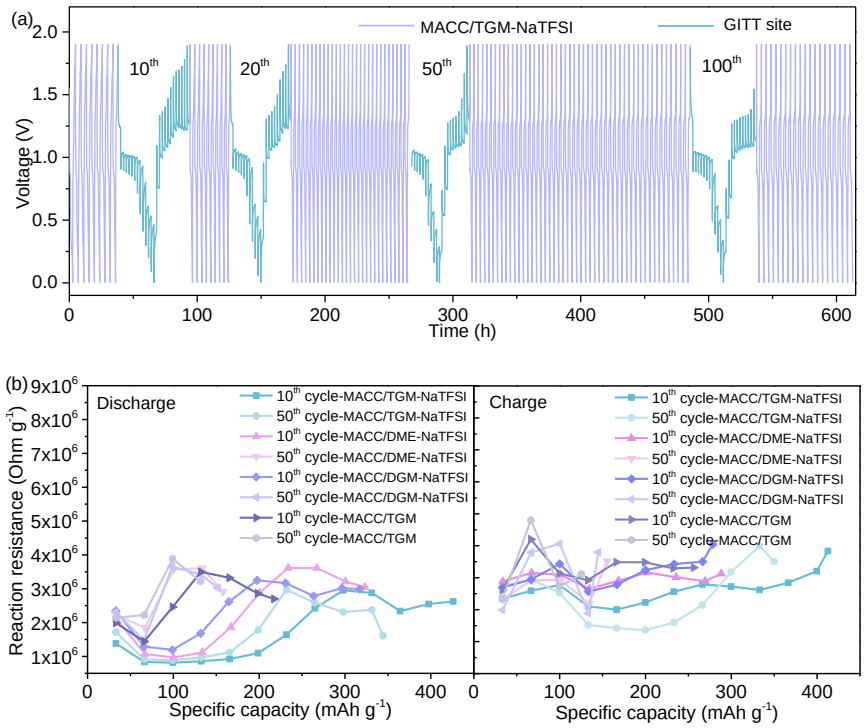

Fig. S15 (a) Voltage *vs* time profiles during the GITT measurement at 0.2 A g^{-1}. (b) *In-situ* reaction resistances of the CNCS cathode using different electrolytes.

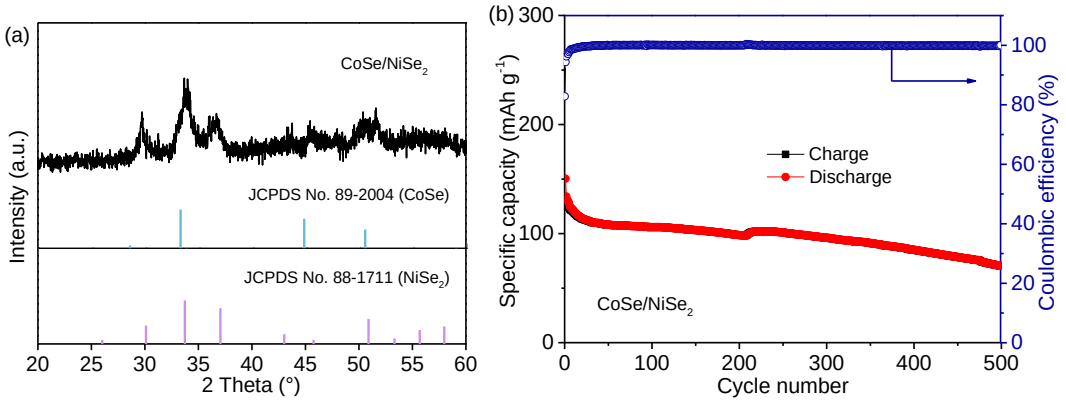

Fig. S16 (a) XRD pattern of binary CoSe/$NiSe_2$ composite. (b) The capacity and Coulombic efficiency of the corresponding composite at 1.0 A g^{-1}. It was activated for 15 cycles at 0.2 A g^{-1}.

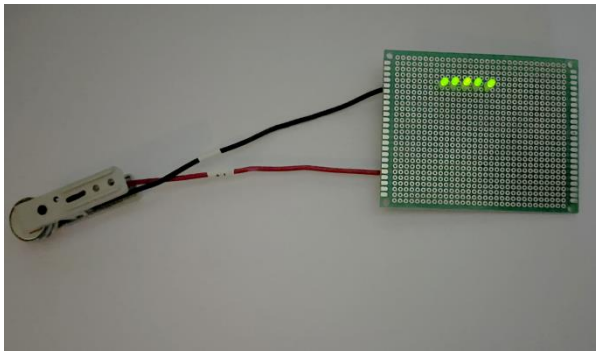

Fig. S17 LED light demonstration powered by the MNHB.

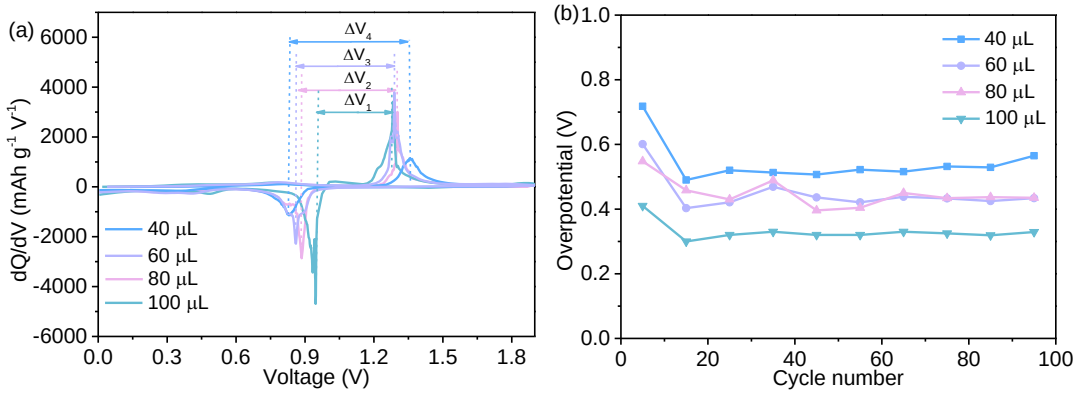

Fig. S18 (a) The dQ/dV plots and (b) overvoltages of CNCS cathodes under different electrolyte contents during the cyclic process.

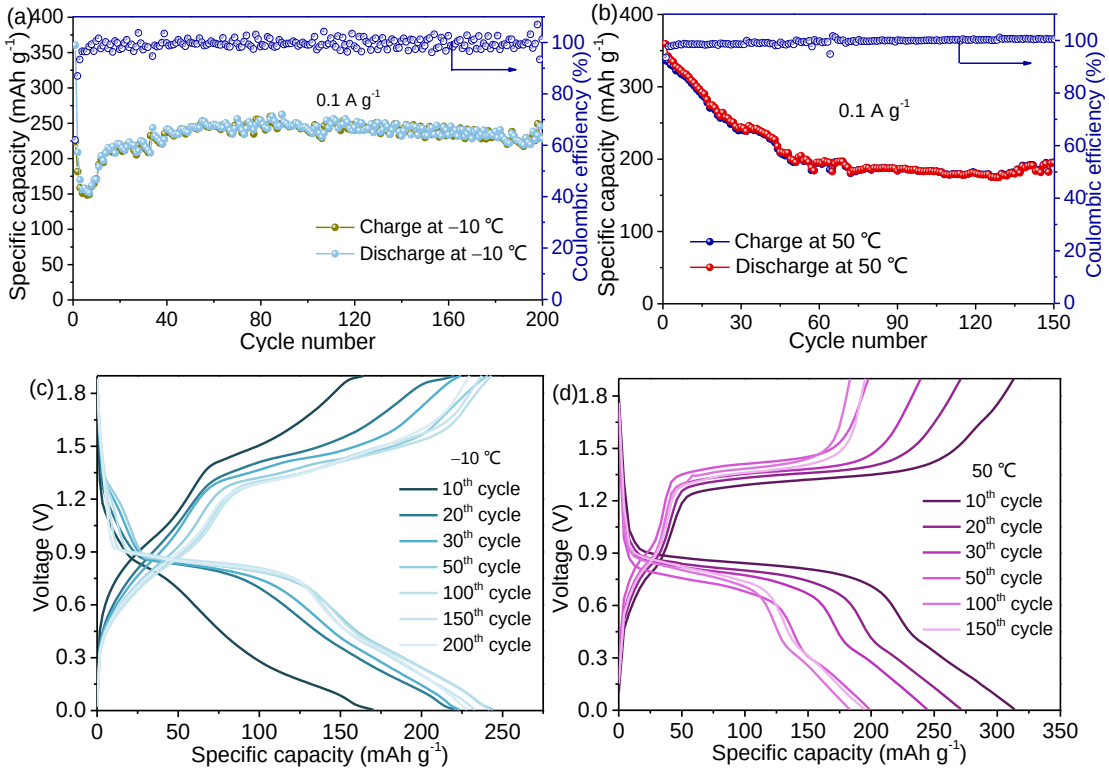

Fig. S19 Cyclic properties at (a) low- and (b) high-temperature conditions. Charge/discharge curves at 0.1 A g^{-1} under (c) low temperature of –10 °C and (d) high temperature of 50 °C.

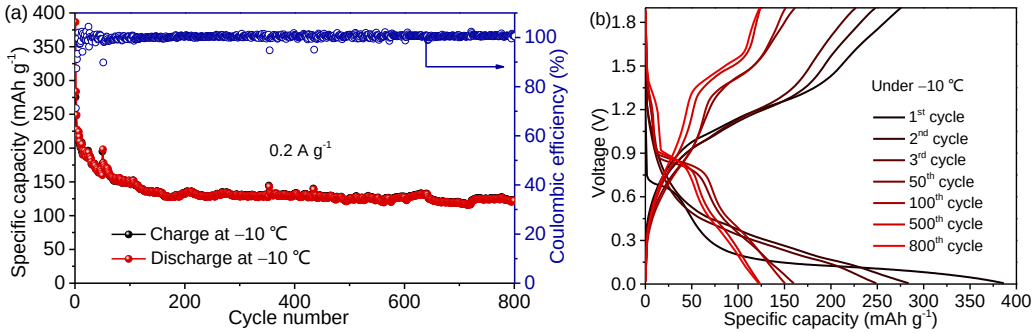

Fig. S20 (a) Cycling performance and (b) charge/discharge curves at 0.2 A g^{-1} under low temperature of –10 °C.

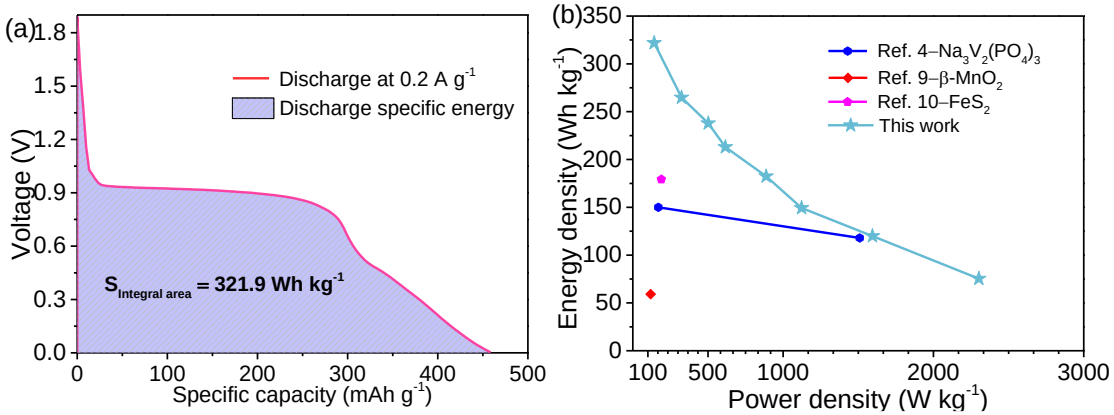

Fig. S21 (a) Calculated energy density of the cell. (b) Power density energy *vs.* energy density for the current work and other works.

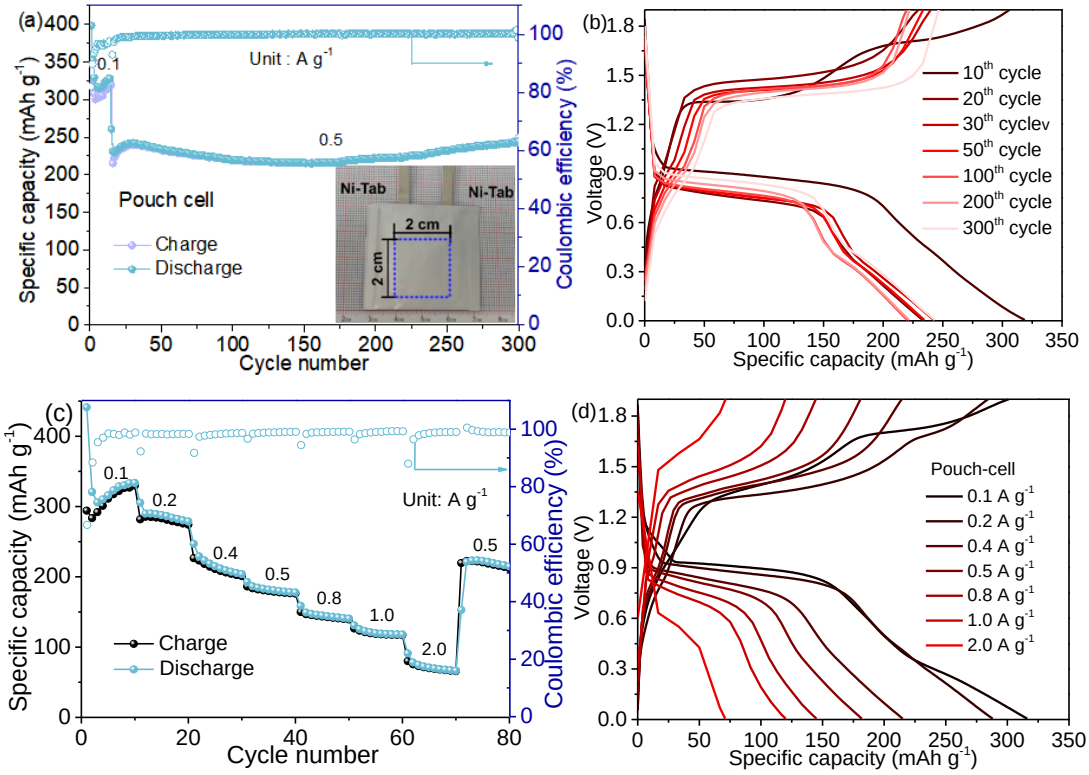

Fig. S22 (a) Long-term cycling performance of pouch cell at 0.5 A g^{-1} using MACC/TGM-NaTFSI as electrolyte. It was activated for 15 cycles at 0.1 A g^{-1}. (b) The charging/discharging profiles. (c) The rate-performance of the pouch cell. (d) Corresponding charging/discharging curves at different rates.

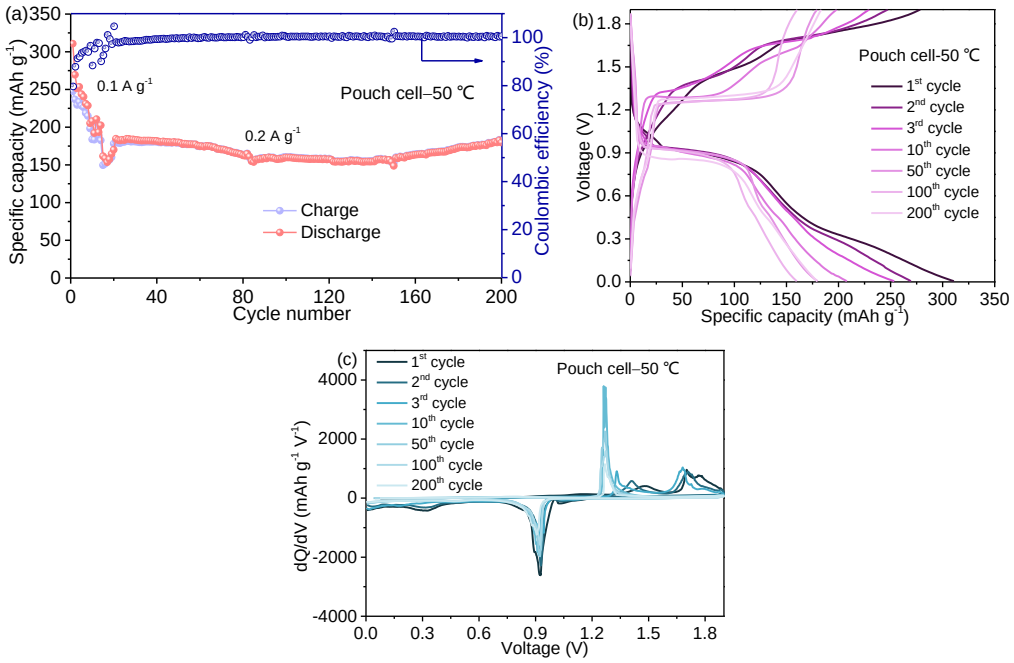

Fig. S23 (a) The long-term cycling performance of the pouch cell with MACC/TGM-

NaTFSI electrolyte at 0.2 A g^{-1} under 50 °C, after activating 15 cycles at 0.1 A g^{-1}. (b,c) Corresponding charging/discharging curves and the dQ/dV plots.

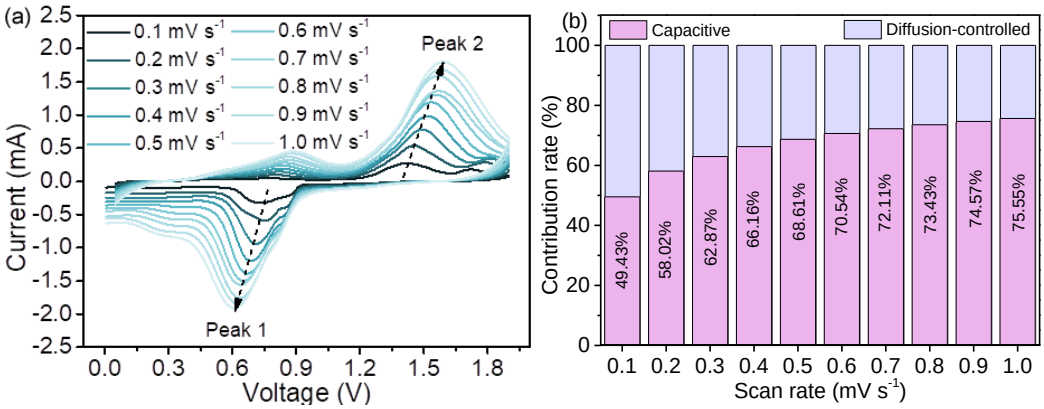

Fig. S24 (a) CV curves at rates from 0.1 to 1.0 mV s^{-1}. (b) The corresponding capacitive and diffusion-controlled contribution rates

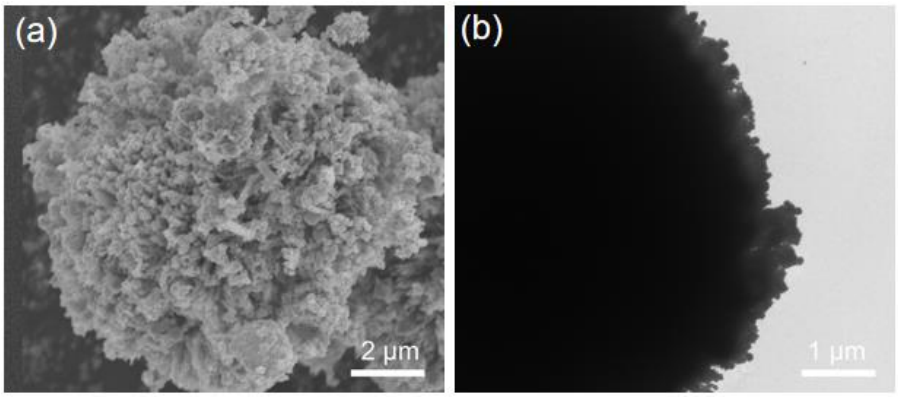

Fig. S25 (a) SEM and (b) TEM images of CNCS after 100 cycles at 0.2 A g^{-1}.

Table S1. Comparison on the rate-performance with other MNHBs.

Cathode	Electrolyte	Cycling rate (A g^{-1})	Capacity (mAh g^{-1})	Ref.
$CoSe/NiSe_2/CuSe_2$	0.2 M $[Mg_2Cl_2][AlCl_4]_2$/TGM-0.4 M NaTFSI	0.2, 0.5, 0.8, 1.0, 1.5, 3.0, 5.0	441.1, 408.7, 378.8, 345.8, 308.4, 265.9, 225.5, 163.7	This work
TiS_2	1.0 M $NaBH_4$ + 0.1 M $Mg(BH_4)_2$/DGM	0.2, 0.5, 1, 2, 4	200, 160, 138, 108, 75	1

$Na_{1.5}VPO_{4.8}F_{0.7}$	2 M $NaBH_4$ + 0.2 M $Mg(BH_4)_2$ in tetraglyme	0.026, 0.13, 0.26	112, 100.5, 80.8	2
TiO_2-B	0.2 M $Mg(BH_4)_2$ + 2 M $NaBH_4$	0.02, 0.05, 0.1, 0.2, 0.5, 1.0	205, 195, 180, 165, 155, 136	3
$Na_3V_2(PO_4)_3$	0.2 M $[Mg_2Cl_2][AlCl_4]_2$/DME-$NaAlCl_4$	0.059, 0.118, 0.236, 0.59, 1.18	100.9, 99, 96, 87, 83	4
Layered VS_2	$Mg(HMDS)_2$ /$AlCl_3$/THF-NaTFSI	0.05, 0.1, 0.2, 0.5, 1.0	185, 170, 150, 125, 100	5
$NaTi_2(PO_4)_3$@C	0.2 M $[Mg_2(m\text{-}Cl)_2][AlCl_4]_2$/ DME + 0.4 M $NaAlCl_4$	0.133, 0.266, 0.665, 1.064, 1.33	125, 110, 105, 101, 57	6
Mg-$NaCrO_2$	Mg-APC	0.006, 0.06, 0.12, 0.24, 0.6	118, 96, 81, 61, 31	7
$FeFe(CN)_6$	$Mg(HMDS)_2$/$AlCl_3$/ DGM-NaTFSI	0.05, 0.1, 0.2, 0.5, 1.0	140, 120, 110, 95, 85	8

References

1 X. F. Bian, Y. Gao, Q. Fu, S. Indris, Y. M. Ju, Y. Meng, F. Du, N. Bramnik, H. Ehrenberg and Y. J. Wei, *J. Mater. Chem. A*, 2017, **5**, 600–608.

2 K. V. Kravchyk, M. Walter and M. V. Kovalenko, *Comm. Chem.,* 2019, **2**, 84.

3 M. Vincent, V. S. Avvaru, M. Haranczyk and V. Etacheri, *Chem. Eng. J.,* 2022, **433**, 133810.

4 Y. F. Li, Q. Y. An, Y. W. Cheng, Y. L. Liang, Y. Ren, C. J. Sun, H. Z. Dong, J. Tang, G. S. Li and Y. Yao, *Nano Energy*, 2017, **34**, 188–194.

5 X. L. Hu, J. B. Peng, F. Xu and M. Y. Ding, *ACS Appl. Mater. Interfaces*, 2021, **13**, 57252−57263.

6 Y. Xu, W. Cao, Y. Yin, J. Sheng, Q. An, Q. Wei, W. Yang and L. Mai, *Nano Energy*, 2019*,* **55**, 526–533.

7 R. G. Zhang, O. Tutusaus, R. Mohtadi and C. Ling, *Front. Chem*., 2018, **6**, 611.

8 Y. J. Zhang, J. W. Shen, X. Li, Z. X. Chen, S. Cao, T. Li and F. Xu, *Phys. Chem. Chem. Phys*., 2019, **21**, 20269–20275.

9 S. N. Zhang, C. L. Zhao, K. Zhu, J. Q. Zhao, Y. Y. Gao, K. Ye, J. Yan, L. Wang and

D. X. Cao, *Energy Environ. Mater.*, 2022, **0**, 1–8.

10 M. Walter, K. V. Kravchyk, M. Ibanez and M. V. Kovalenko, *Chem. Mater.*, 2015, **27**, 7452–7458.